

Detecting Hallucinations in Virtual Histology with Neural Precursors

Ji-Hun Oh[†] Kianoush Falahkheirkhah[†] Rohit Bhargava^{†, ‡}

[†]University of Illinois Urbana-Champaign, Urbana, IL, USA

[‡]CZ Biohub Chicago, LLC, Chicago, IL, USA

{jihunoh2, kf4, rxb}@illinois.edu

Abstract

Significant biomedical research and clinical care rely on the histopathologic examination of tissue structure using microscopy of stained tissue. Virtual staining (VS) offers a promising alternative with the potential to reduce cost and eliminate the use of toxic reagents. However, the critical challenge of hallucinations limits confidence in its use, necessitating a VS co-pilot to detect these hallucinations. Here, we first formally establish the problem of hallucination detection in VS. Next, we introduce a scalable, post-hoc hallucination detection method that identifies a Neural Hallucination Precursor (NHP) from VS model embeddings for test-time detection. We report extensive validation across diverse and challenging VS settings to demonstrate NHP’s effectiveness and robustness. Furthermore, we show that VS models with fewer hallucinations do not necessarily disclose them better, risking a false sense of security when reporting just the former metric. This highlights the need for a reassessment of current VS evaluation practices.

1 Introduction

Histopathology is practice of determining disease from optical images of human tissue. After staining by special dyes like hematoxylin and eosin (HE) to highlight structures, pathologists examine the sample under a microscope to identify patterns of deviation from healthy tissues. Specific cellular and tissue patterns indicate severity of the disease and decide treatment options [1]. Although this process has been well-established over the last 125 years as the standard means to diagnose most diseases, especially cancer, staining remains labor-intensive and costly. These issues are exacerbated by the need for multiple staining as

a single stain cannot reveal all information for accurate diagnosis. Recently, image-to-image translation (I2IT) methods have emerged as a promising alternative, generating realistic stained images from different stains or label-free (*i.e.*, stain-free) modalities [2, 3, 4, 5, 6, 7, 8, 9, 10, 11, 12, 13, 14, 15, 16, 17, 18, 19, 20, 21, 22]. Termed virtual staining (VS), this approach offers faster assessment of tissues, at lower cost and with simpler workflows, thereby streamlining medical care for patients.

However, VS models are known to “hallucinate” (Fig. 1), producing false histopathological patterns that can mislead clinicians. This poses deadly risk in high-stake healthcare settings through misdiagnosis. This highlights

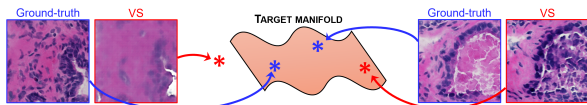


Figure 1: Hallucination examples. Symptoms can be transparent (left) or realistic (right). The latter is particularly challenging to identify as the hallucination is within the target data manifold.

the need for a hallucination detector (or monitor) to serve as a co-pilot to VS to guide clinicians away from ill-decisions and uphold VS trustworthiness. Despite its clinical value, this task received little attention, with just two recent noteworthy preprints [23, 24] addressing it. However, we notice some shortcomings in detection validation (with limited scope or misguided protocols) and method (particularly on scalability and robustness), detailed in §2.2.¹ The former issue is critical as erroneous practices—even minor ones—can skew the objective evaluation of detection performance. The latter issue is critical because—(i) VS is applied to whole slide images (WSIs), which can range into TB sizes, and (ii) VS datasets are diverse, covering different organs, stain and label-free techniques, and I2IT methods. These challenges demand a detector with high throughput and versatility.

In this work, we address the first issue by clearly establishing the detection problem and its evaluation (§3). We explore hallucination causes to clarify what hallucination detection is and isn’t, namely underscoring that it is neither an out-of-distribution (OOD) nor outlier problem. Instead, it must align with VS prediction. We then address the second issue by proposing a hallucination detector dubbed Neural Hallucination Precursor (NHP, §4). Briefly, NHP performs a post-hoc search for the optimal marker in the VS model’s embedded space by merging fea-

ture signals and self-tuning all relevant performance parameters. This meets the scalability and versatility requirements. We show in §5 that NHP performs well irrespective of organ type, source/target pair (encompassing HE; immunohistochemistry, IHC; immunofluorescence, IF; and label-free stimulated Raman scattering, SRS), and I2IT backbone (supervised and unsupervised). We further contribute by introducing new research themes to the broader VS community—these include adversarial attacks, and the interplay (or lack thereof) between hallucination robustness and detection to highlight the dangers of solely reporting one type of safety metric.

2 Related Work

2.1 Virtual Staining

The I2IT paradigm of VS can be either supervised, using source/target pairs from multiplexing or label-free modalities [17, 18, 19, 20, 22, 3], or unsupervised, using unpaired sets [8, 6, 9, 4, 7]. Supervised I2IT methods perform better but suffer from technological overhead. An emerging trend is to use adjacent tissue slices as source/target, meticulously registered [11, 13, 14, 5, 10, 12]. Their proximity introduces a degree of perceptual similarity, sometimes termed an “inconsistent pair”; traditional supervised methods remain elusive due to pixel misalignment, but the inconsistent pair is accepted for full-reference evaluations. Overall, GANs are the dominant I2IT approach in VS, with Pix2Pix [25] in supervised settings and CycleGAN [26] in unsupervised ones.

In this work, we consider both supervised and unsupervised GAN-based VS tasks. As mentioned later, we require at least inconsistent pairs to define hallucinations, limiting our latter experiments to inconsistently paired datasets, even though they are trained in an unsupervised manner.

¹Based on arXiv submissions prior to Oct. 2024.

2.2 Hallucination Detection in VS

Two recent studies have tackled hallucination detection specifically for VS. Ref. [23] performed cyclic translations between source (autofluorescence) and target (HE) domains to define a hallucination score for lung and kidney biopsies. However, this approach incurs latency and is restricted to GANs yielding the inverse target-to-source model, requiring its additional training otherwise. Another study [24] used the discriminator to monitor HE-to-IHC VS in pediatric Crohn’s disease. While these studies adopt anomaly detection methods exploiting the GAN framework [27, 28, 29], we posit that hallucination precursors exist in the neural embeddings of the VS generator before their manifestation. We show later that our NHP method built upon this premise is significantly more robust. Additionally, the validation of these studies are primarily visual or limited. For instance, [23] distinguished between “good” and “poor” VS models based on training status—while hallucinations are more common in latter, well-trained models are not immune to them. Similarly, flagging corrupted source images [24] may not reliably indicate hallucinations when the VS model is robust. Recognizing these limitations, we aim to provide a more accurate and objective study.

Apart from these studies, mainstream VS literature seeks to mitigate hallucinations by preserving pathological semantics [4, 6, 7, 9, 10, 16, 11, 12, 13, 14]. In contrast, our goal is to detect hallucinations, irrespective of frequency. These goals can be mutually inclusive, but our primary focus here is on detection.

3 Problem Formulation

3.1 Hallucination Definition

VS estimates the I2IT mapping function $G : S \rightarrow T$, for source and target domains S and

T . Let us denote a dataset \mathcal{D} with marginal distributions P_S and P_T for S and T . We apply empirical risk minimization (ERM) to find $\hat{G} \triangleq \arg \min_{\hat{G} \in H} \mathcal{L}(\hat{G}, \mathcal{D})$, where \mathcal{L} is the Nash equilibrium loss of the GAN, and H is the hypothesis space. We drop auxiliary notations like the discriminator.

Hallucination hypothesis. A sample $(s, t) \in S \times T$ with $\hat{G}(s)$ that “conflicts” with t is termed a hallucination. This is a necessary detail to define the problem but is ill-defined. While studies in inverse medical imaging [31, 32] put forth hallucination indexes, they are unsuitable herein due to their assumptions about data linearity and stochastic models. In what follows, we use popular full-reference (FR)² image similarity metrics \mathcal{Q} from recent VS papers: Peak Signal-to-Noise Ratio (PSNR) in [8, 5, 4, 16, 6, 12, 14, 15], Multi-Scale Structural Similarity Index (MS-SSIM) [33] in [11, 5, 10, 4, 16, 6, 12, 17, 14, 15], and Learned Perceptual Image Patch Similarity (LPIPS) [34] in [11]. For consistency, we use 1-LPIPS, ensuring $\mathcal{Q}(\hat{G}(s), t) \leq 1, \forall \mathcal{Q}$, with lower values indicating hallucinations. This allows hallucination definitions only on fully (or at least inconsistently) paired data, both denoting target by t for notation simplicity. A statistical analysis of these metrics on an SRS-to-HE VS experiment (from §5.1) showed that Kendall’s τ [35] is roughly 0.4-0.5 among one another, indicating moderate-to-strong rank consistency. Note, pathologist evaluations are impractical for large-scale studies such as ours due to high cost and variability.

3.2 Hallucination Causes

Hallucinations stem from the rudimentary failure of \hat{G} to emulate G , influenced by several factors delineated by the VS pipeline (Fig. 2).

²No-reference (NR) compares $\hat{G}(s)$ to P_T , which cannot assay realistic hallucinations when $\hat{G}(s) \in P_T$. Thus, FR is essential.

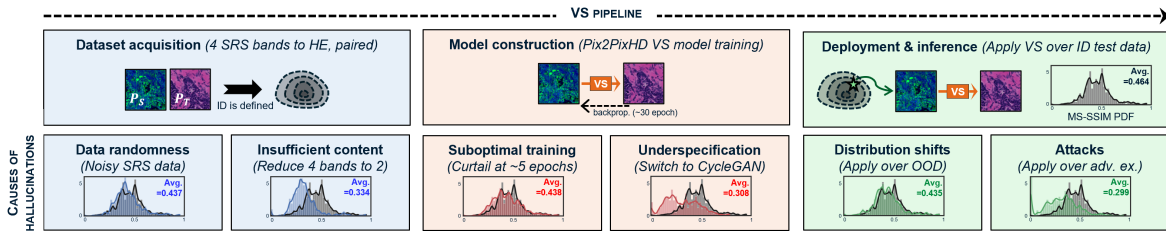


Figure 2: Hallucination causes. We confirm each factor by ablating specific components (bottom row) in the VS pipeline and observing the resultant drop in MS-SSIM. The adopted experiment is from §5: VS of HE (target) from 4 SRS bands (source), trained by Pix2PixHD [30] and evaluated over an ID test set. OOD and adversarial example details in §5.3. Similar results were seen with PSNR and LPIPS.

Briefly, we discuss them, while also providing an empirical demonstration of these factors in an SRS-to-HE VS experiment in Fig. 2.

(i) From data: G is nondeterministic for aleatoric data [36, 37, 38, 39]. This includes randomness in the generating process (*e.g.*, measurement noise) or insufficient source domain content (*e.g.*, low resolution). Such intrinsic ill-posedness leads to one-to-many translations for $G(s)$, where plausible translations may not match true observations, causing hallucinations. (ii) From training: $\hat{G} \neq G$ due to training difficulties of GANs [40, 41], exacerbated by issues like class imbalance [42] and asymmetric domains [43]. Even without these issues, underspecification [44, 45] leads to infinite candidate solutions (*aka* Rashomon set [46], $H^* \subset H$) equivalently describing the data, where $\mathcal{L}_{\text{val}}(\hat{G}, \mathcal{D}) < \tau$, $\forall \hat{G} \in H^*$, with \mathcal{L}_{val} as a validation criteria, and τ a threshold. The realized solution from H^* may not match G as there is no theoretical favor towards it. This is pronounced in small datasets or under-constrained I2IT, notably unsupervised ones [47, 48, 49]. (iii) From inference: In histopathology, the *i.i.d.* assumption for training and test data is easily violated due to long-tailed and heterogeneous distributions. This leads to out-of-distribution (OOD) encounters where $s \notin P_S$ (*cf.*, in-distribution, ID, $s \in P_S$). Examples are institute or popula-

tion shifts [50], or unseen artifacts or pathologies [51]. VS models are prone to hallucinate over OOD, a ramification of underspecification: ERM only constrains ID behavior, resulting in many H^* members exhibiting poor OOD generalization [52, 45, 53]. In addition, cybersecurity is highly relevant for digital pathology [54]. Unfortunately, I2IT models lack adversarial robustness, with research showing that injecting imperceptible noise disrupts malicious applications like deepfake [55, 56] and watermark removers [57]. This hints that VS models too can be attacked with hallucination intent.

3.3 Hallucination Detection Objective

Acknowledging these vast factors, we aim to construct a monitor $f : S \rightarrow \mathbb{R}$ returning the VS prediction confidence. This monitor should ideally correlate with $\mathcal{Q}(\hat{G}(s), t)$ and operate blindly, without prior knowledge of t .

Evaluation metric. In real world applications, monitors are deployed in binary form—accept if $f(s) \geq \lambda$ (a threshold), otherwise reject. An effective monitor should preferentially reject hallucinations to maintain the fidelity of accepted images. Inspired by [58, 59, 60], we evaluate hallucination detection performance as follows: For a test set $\mathcal{D}_{\text{test}}$, we set threshold λ_p to reject $p\%$ of samples, satisfying

$\Pr_{(s,t) \in \mathcal{D}_{\text{test}}} [f(s) \geq \lambda_p] = 1 - p$, and compute the average hallucination magnitude of non-rejected samples. To sidestep the sensitivity of p , we sweep $p \in [0, 1)$ and measure the area-under-curve (AUC):

$$AUC_f \triangleq \int_0^1 \mathbb{E}_{(s,t) \in \mathcal{D}_{\text{test}} | f(s) \geq \lambda_p} [\mathcal{Q}(\hat{G}(s), t)] dp. \quad (1)$$

While this metric reflects monitor performance, it is biased towards VS models with better base performance. To adjust for this, we normalize w.r.t. the AUCs of a random monitor and an ‘oracle’. The former assigns accept/reject decisions randomly, yielding an AUC equivalent to $\mathbb{E}_{(s,t) \in \mathcal{D}_{\text{test}}} [\mathcal{Q}(\hat{G}(s), t)]$. The oracle’s AUC represents the hypothetical theoretical upper bound, calculated using $\mathcal{Q}(\hat{G}(s), t)$ as the confidence. Our final metric, coined Hallucination Rejection Preference (HRP), is defined as:

$$HRP \triangleq \frac{(AUC_f - AUC_{\text{random}})}{(AUC_{\text{oracle}} - AUC_{\text{random}})}. \quad (2)$$

A higher HRP value approaching 1 indicates better monitor performance, computed separately for each \mathcal{Q} metric. Note, simultaneously achieving maximal (=1) HRP on all metrics is infeasible, as this would require the monitor to perfectly align with the rankings of multiple metrics, which is impossible due to Kendall’s $\tau \neq 1$.

3.4 Hallucination vs. OOD Detection

The mainstream detection problem of OOD (including sub-categories like anomaly and novelty) focuses on differentiating OOD from ID [61]. While one might confound hallucination detection as an OOD task, §3.2 highlights critical issues suggesting otherwise: (i) There is a conflict with generalization as not all OOD pose a risk due to robustness. For instance,

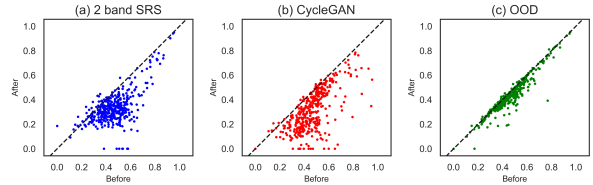


Figure 3: The data dependency of hallucinogenic factors. We plot the MS-SSIM per sample in Fig. 2 before (x-axis) vs. after (y-axis) select ablations: (a) reducing SRS source content from 4 to 2 bands, (b) underspecification by switching Pix2PixHD with CycleGAN [26], (c) shifting the ID test data to become OOD.

the mean MS-SSIM only dropped from 0.464 to 0.435 when switching from ID to OOD test data (Fig. 2). Fig. 3-c further illustrates the sample-dependent effects of these shifts, suggesting that we should aim to detect just its fatal cases. Otherwise, we raise excessive flags and compromise the open-world applicability of VS. (ii) ID is not hallucination-safe, as it can arise from domain-agnostic factors like data ambiguity, suboptimal training, Rashomon effect, and attacks. This is supported by the significant overlap in MS-SSIM PDFs between ID and OOD test sets (Fig. 2). In fact, hallucinations even occur within training data.

Note, similar arguments have been raised in image classification [62, 63, 64, 65]. A key distinction though lies in semantic OOD (*i.e.*, novelty). In classification, the clear-cut closed label set during training mandates the detection of semantic OODs without exception, which fall outside the classifier’s scope. However, VS involves image generation, void of such constraints with outputs capable of expressing any image. Thus, it is feasible to be accurate over semantic OODs. A recent large-scale study on VS generalization [66] proved this with novel phenotypes and cell types, suggesting that semantic OOD should be treated like other OOD types. Furthermore, ID hallucinations might mislead one to

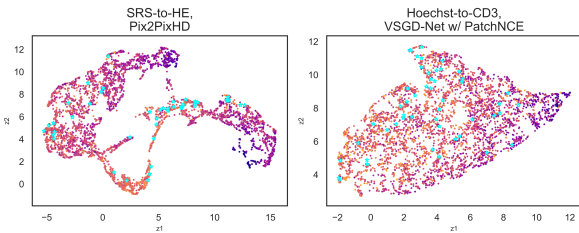


Figure 4: UMAP of ID embeddings. We visualize the Uniform Manifold Approximation and Projection (UMAP) [67] of the VS model embeddings for ID. In addition to the SRS-to-HE experiment in Fig. 2 (left), we also show a HO342-to-CD3 case from §5 (right). Color code reflects **low/high** MS-SSIM, with top hallucinatory instances (lowest MS-SSIM) marked by \star . Note how outliers are not necessarily hallucinations and vice versa.

think this is an outlier issue, which do not discern ID/OOD and simply refer to abnormalities w.r.t. the bulk of the data—*i.e.*, inlier IDs are non-hallucinatory and only outliers hallucinate. However, as discussed, most hallucinogenic factors are distribution-agnostic, refuting this notion. We further validate this in Fig. 4.

Lastly, much of these discussions extend to other factors: hallucination detection is not merely an, *e.g.*, ambiguity or underspecified problem (Fig. 3-a and -b). While they contribute to hallucinations, they are neither necessary nor sufficient conditions on their own. Hence, hallucination detection (and its evaluation) should not focus solely on criteria latent to these factors, but instead align with VS predictions—detecting if *and only if* $\mathcal{Q}(\hat{G}(s), t)$ is poor.

4 Method

We present our NHP monitor leveraging embedded neural signals from the trained VS model, specifically the k^{th} nearest neighbor (KNN) method, to score confidence.

Assumptions. (i) We operate in a white-box setting, accessing intermediate layers of

the VS model, a common premise in literature [68, 69, 70, 71, 72, 73, 74, 75, 76, 77, 59]. (ii) We assume access to a fully or inconsistently paired dataset, \mathcal{D}^* , for monitor calibration. If permitted, it may be conveniently drawn from the training set, $\mathcal{D}^* \subseteq \mathcal{D}$. We assume this henceforth as it applies to our study (recall, we focus on fully- and inconsistently-paired datasets). These assumptions are reasonable in clinical settings as the developer of the monitor and the VS model are usually the same.

4.1 Formulation

Let $s \in S$ be a sample for hallucination assessment. Denoting by $\hat{G}^l(\cdot) \in \mathbb{R}^{C \times H \times W}$ the l -th layer CNN block of the VS model, we extract the feature vector, $z^l \in \mathbb{R}^C$, with

$$z_c^l \triangleq \frac{1}{HW} \sum_h \sum_w \hat{G}_{c,h,w}^l(s), \quad (3)$$

$$\forall c \in \{1, 2, \dots, C\}.$$

Our confidence scoring function utilizes two feature signals: the (i) feature norm (FN), computed by the ℓ_2 norm:

$$FN \triangleq \|z^l\|_2, \quad (4)$$

and the (ii) KNN feature distance to a bank of “safe” samples in \mathcal{D}^* , devoid of hallucinations. We define this subset based on a truncation intensity $q \in [0, 1]$:

$$\mathcal{D}_q^* \triangleq \{(s^*, t^*) \in \mathcal{D}^* \mid \mathcal{Q}(\hat{G}(s^*), t^*) \geq \lambda_{\mathcal{Q},q}, \forall \mathcal{Q}\}, \quad (5)$$

where, for each \mathcal{Q} metric, the threshold $\lambda_{\mathcal{Q},q}$ satisfies $\Pr_{(s^*, t^*) \in \mathcal{D}^*}[\mathcal{Q}(\hat{G}(s^*), t^*) \geq \lambda_{\mathcal{Q},q}] = 1 - q$. It holds that $\mathcal{D}_q^* \subseteq \mathcal{D}^*$, with equality at $q = 0$. Letting Z_q^{*l} be the feature set of samples in \mathcal{D}_q^* , we aggregate normalized Euclidean distances between z^l and $z^{*l} \in Z_q^{*l}$ as

follows:

$$r(z^l; Z_q^{*l}) \triangleq \left\{ \left\| \frac{z^l}{\|z^l\|_2} - \frac{z^{*l}}{\|z^{*l}\|_2} \right\|_2 \mid \forall z^{*l} \in Z_q^{*l} \right\}. \quad (6)$$

The normalization helps decouple FN. We reorder this set in ascending order, denoting by $\{r_{(i)}(z^l; Z_q^{*l})\}_{i=1}^n$ such that the reordered index satisfy $r_{(1)}(z^l; Z_q^{*l}) \leq r_{(2)}(z^l; Z_q^{*l}) \leq \dots \leq r_{(n)}(z^l; Z_q^{*l})$. We take the negative of the k^{th} index:

$$KNN \triangleq -r_{(k)}(z^l; Z_q^{*l}). \quad (7)$$

Finally, we integrate these signals to form our confidence scoring function:

$$f_{\text{NHP}}(s; \hat{G}, \mathcal{D}^*, l, q, k, \gamma) \triangleq KNN \times FN^\gamma, \quad (8)$$

where γ acts as a balance coefficient. With this configuration, we certify lower confidence (higher hallucination threat) when a sample’s feature is distant from the non-hallucinatory portion of \mathcal{D}^* , adjusted by FN.

Apart from \hat{G} and \mathcal{D}^* , we rely on four parameters: $\{l, q, k, \gamma\}$. To tune these, we reserve a portion of \mathcal{D}^* for validation and perform a grid search to maximize average HRP on this held-out subset. Note, hallucinations are not removed (as per Eq. 5) for this set. We call this method “self-tuning” as \mathcal{D}^* is subsampled from the training set in our work. Self-tuning essentially relies on the hypothesis that a monitor effective over the training set holds across unseen data. NHP is shown in Fig. 5.

4.2 Motivation of NHP’s Design

NHP adopts the KNN-based detector in [68], recovering the vanilla formulation when setting l to the penultimate layer and $q = \gamma = 0$. These design choices are well-justified for semantic OOD detection in image classifiers. For instance, empirical studies show that deeper layers reflect image semantics [68, 69, 74, 75, 76, 77, 59], with ID data exhibiting higher FN values [70, 71, 68, 72, 73], prompting the need

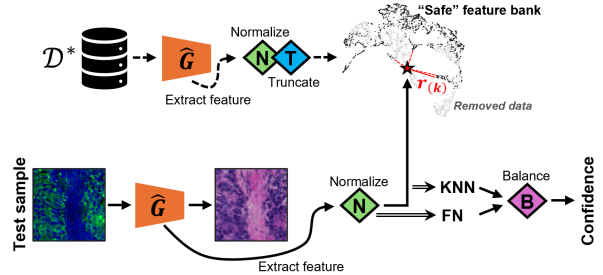


Figure 5: Schematic pipeline of NHP. The hallucination-free feature bank and NHP parameters are determined beforehand using a calibration dataset, which may be sampled from the training set. During VS inference, we extract the feature, compute FN and KNN, and balance them per Eq. 8 to estimate the VS prediction confidence.

to decouple it ($\gamma = 0$) to maintain higher confidence for ID, as per Eq. 7. Under the ID/OOD dichotomy, it also makes sense to use the entire \mathcal{D}^* ($q = 0$) as all samples are unequivocally ID when drawn from training.

However, we speculate that these choices are suboptimal for VS due to contextual differences in task type (image classification *vs.* I2IT) and detection goal (OOD *vs.* hallucinations, §3.4). For instance, there is no evidence of higher FN for ID in VS; recent work [73] linked FN to the maximum logit under a regularity condition, but this does not apply in non-classification contexts like I2IT. Nor is this behavior desired, as IDs are not exempt from hallucination detection. Likewise, ID status alone does not ensure a safe bank, requiring explicit truncation. In addition, hallucinations are not strictly semantic, challenging the norm of using deeper bottleneck layers. Arguably, the optimal hyperparameters in our context are unknown. We further hypothesize that every VS model is unique, meaning no single parameter set is optimal across all VS datasets and I2IT architectures. Hence, the core modification of NHP is that we opt for the most flexible and agnostic formulation via Eq. 8, and through

self-tuning, we tune all performance parameters to adapt to each VS application.

4.3 Advantages

Owing the above, NHP is effective and robust. Moreover, self-tuning leverages the hallucinations within ID training set, obviating the need for advanced tuning schemes (*cf.* in OOD detection, many works create pseudo OOD data, *e.g.*, jigsaw puzzles [78, 72]). In addition, NHP is highly scalable, imposing minimal training and inference burdens; no training addition or changes is needed, while requiring only a single forward pass during testing. The only overhead is a grid search, executable in just a few minutes on a commercial CPU (97 seconds on an i9-9900KF in our work) using Faiss’s KNN algorithm [79], and inference time is negligible (throughput of <1 ms per 100 image patches). These times are significantly faster than the VS model training (3+ hours on a V100 GPU) and inference (~ 3 seconds per 100 patches). While it requires storing the feature bank of \mathcal{D}_q^* , it remains effective with banks under 1K samples with less than 1MB memory.

5 Experiments, Results, and Discussion

5.1 Experimental Settings

We verify NHP’s effectiveness in detecting hallucinations across various VS settings, described below.

Datasets. We consider seven VS tasks: (i) In-house SRS data in prostate cancer (PCa) translating to HE. We conduct SRS imaging at four Raman shift frequencies of 2847, 2879, 2933, and 2979 cm^{-1} , corresponding to four image channels. Afterwards, the tissue sections were HE-stained and digitized at 20x magnification using Nanozoomer scanners. The SRS and HE WSIs were registered, split by

patient for training/testing, and divided into patches. This dataset was acquired in collaboration with Mayo Clinic, Rochester, MN, with full details in [80]. (ii) Hoechst 33342 (HO342) IF dataset [22] translating to T-cell subtype indicators, CD3 and CD8, in clear cell renal cell carcinoma (ccRCC). (iii) MIST dataset [10] translating HE to four IHC stains in breast cancer (BC): ER, HER2, PR, and Ki67. The SRS and HO342 datasets are paired, while MIST is inconsistently paired. All experiments use 256×256 pixel² patches (tessellated for MIST, which is in 1024×1024 pixel²), resulting in approximately 4K, 404K, and 69K training samples for SRS, HO342, MIST, respectively. These datasets cover diverse cancer (PCa, BC, ccRCC), dataset sizes (4-475K), and imaging modalities (HE, IHCs, IFs, label-free SRS).

I2IT methods. For paired datasets, we consider the supervised (i) Pix2PixHD [30], and advanced techniques like the VSGD [15] model with the PatchNCE [81] loss, which we term (ii) VSGD+pNCE. For inconsistently paired datasets, we assess two distinct unsupervised methods: (iii) CycleGAN [26] and (iv) CUT [82]. These amount to 7×2 VS settings, each run 10 times with different seeds, totaling 140 VS models. Implementations follow official repositories. For SRS, all models are trained with a batch size of 8 and a learning rate of 0.002 for 30 epochs, linearly decaying to zero over the last 15 epochs. For HO342, all models use a learning rate of 0.0002, batch size of 8, and train for 1 epoch. On MIST, all models train with a batch size of 1, learning rate of 0.0002, and 10 epochs.

Evaluation metrics. Over the test set, we independently compute the HRP using PSNR, MS-SSIM, and LPIPS, but report their mean due to space constraints.

NHP implementation details. For grid search, we explore: (i) $l \in \{0, 0.25, 0.5, 0.75, 1\}$, where indexes denote the depth ratio, *e.g.*,

Table 1: HRP (% , \uparrow) results across diverse VS settings. For GAN-based anomaly detectors, we display mean (\pm std.) over 10 runs; for NHP configs, it is over 100 results–10 runs, each with 10 self-tuning validation splits. Best method in **bold**, while the runner-up underlined.

Method	SRS-to-HE		HO342-to-CD3		HO342-to-CD8		HE-to-ER		HE-to-HER2		HE-to-PR		HE-to-Ki67		Avg.
	Pix2PixHD	VSGD+pNCE	Pix2PixHD	VSGD+pNCE	Pix2PixHD	VSGD+pNCE	CycleGAN	CUT	CycleGAN	CUT	CycleGAN	CUT	CycleGAN	CUT	
GAN-BASED ANOMALY DETECTION															
ALOCC	-33.22 \pm 10.3	-0.38 \pm 20.83	-30.8 \pm 4.83	15.61 \pm 16.96	-7.46 \pm 9.05	15.69 \pm 19.96	2.99 \pm 44.22	0.56 \pm 26.08	11.78 \pm 24.42	3.16 \pm 26.15	9.39 \pm 46.25	-25.88 \pm 12.54	24.8 \pm 20.42	3.95 \pm 29.42	-0.7
ALAD	-	-	-	-	-	-	-6.8 \pm 8.99	-	-7.02 \pm 14.97	-	-3.86 \pm 12.31	-	2.5 \pm 22.81	-	-3.8
F-AnoGAN _{res.}	-	-	-	-	-	-	3.85 \pm 7.62	-	-4.13 \pm 7.12	-	4.76 \pm 3.41	-	8.56 \pm 5.92	-	3.26
NHP ABLATIONS OVER KNN SETUP															
NHP ($\gamma = 0$)	40.7 \pm 8.45	<u>36.66\pm5.84</u>	40.29 \pm 3.38	49.33 \pm 16.86	24.2 \pm 5.27	30.65 \pm 14.77	68.03 \pm 3.09	56.42 \pm 5.32	50.14 \pm 5.1	42.79 \pm 8.5	<u>68.64\pm1.93</u>	53.99 \pm 5.3	66.74 \pm 3.52	40.91 \pm 18.87	47.82
NHP ($q = 0$)	21.44 \pm 13.01	18.33 \pm 10.78	50.49 \pm 1.08	47.23 \pm 15.17	43.62 \pm 5.12	30.88 \pm 13.87	47.71 \pm 3.83	41.91 \pm 14.59	42.19 \pm 6.69	24.41 \pm 7.78	57.37 \pm 3.96	41.34 \pm 10.25	57.41 \pm 4.6	37.61 \pm 22.02	40.14
NHP (linear)	40.7 \pm 8.45	<u>36.66\pm5.84</u>	50.59 \pm 4.81	49.37 \pm 15.65	42.56 \pm 7.99	33.31 \pm 15.99	70.51\pm2.61	61.6 \pm 6.9	50.6 \pm 5.37	42.93 \pm 9.29	68.6 \pm 1.98	<u>57.24\pm4.94</u>	67.14\pm3.69	50.36\pm17.35	<u>51.58</u>
NHP ABLATIONS BY DIFFERENT DISTANCE MEASURES															
NHP (OtB)	13.07 \pm 9.27	34.8 \pm 8.88	40.54 \pm 5.57	39.89 \pm 13.85	29.36 \pm 9.69	27.87 \pm 12.09	61.11 \pm 2.16	49.51 \pm 4.34	45.03 \pm 4.26	35.05 \pm 9.32	63.88 \pm 2.57	51.49 \pm 4.93	61.69 \pm 3.05	38.66 \pm 15.99	42.28
NHP (Res.)	12.02 \pm 17.01	2.75 \pm 17.28	53.06\pm1.54	49.25 \pm 16.24	47.66\pm3.04	32.52 \pm 18.07	37.68 \pm 7.54	30.09 \pm 19.75	46.38 \pm 7.6	22.39 \pm 8.58	48.03 \pm 6.4	31.7 \pm 21.86	61.11 \pm 5.43	47.47 \pm 15.43	37.29
NHP (GMM)	49.04 \pm 5.54	28.73 \pm 9.94	41.61 \pm 3.99	49.53\pm16.94	33.57 \pm 6.51	32.04 \pm 14.03	66.71 \pm 2.01	58.27 \pm 5.13	<u>50.74\pm5.34</u>	43.93\pm8.18	68.51 \pm 2.36	54.75 \pm 6.62	65.42 \pm 3.14	42.17 \pm 22.87	48.93
NHP	49.32\pm5.51	37.24\pm6.74	<u>51.07\pm4.55</u>	<u>49.45\pm15.44</u>	<u>45.65\pm6.09</u>	33.5\pm15.94	<u>69.25\pm2.86</u>	62.15\pm6.31	51.0\pm5.47	<u>43.38\pm8.93</u>	68.87\pm1.87	57.76\pm4.51	<u>67.0\pm3.63</u>	<u>47.91\pm20.45</u>	52.40

0 is the first layer coinciding to the shallowest feature, whereas 1 is the penultimate layer; (ii) $q \in \{0, 0.25, 0.5, 0.75\}$; (iii) $k \in \{1, 10, 25, 50, 100, 200\}$; (iv) $\gamma \in [-10, 10]$ in steps of 0.5. For \mathcal{D}^* , we use the entire SRS training set and stratified 1% and 10% subsets for HO342 and MIST, respectively, yielding approximately 3-7K samples for every experiment. Each 140 VS run evaluates NHP 10 times with different validation splits (25%) for self-tunings, totaling 1400 NHP counts.

Baseline and ablation detectors. We compare with GAN-based anomaly detection methods, the basis of recent VS hallucination detection studies [23, 24]: (i) ALOCC [28, 83] uses the output of the trained target domain discriminator. Without loss of generality, we denote this discriminator(s) by $\hat{D}_T = \{\hat{D}_{T,1}, \hat{D}_{T,2}, \dots, \hat{D}_{T,N}\}$, and define confidence by $\frac{1}{N} \sum_{n=1}^N \hat{D}_{T,n}(\hat{G}(s))$. (ii) ALAD [27] uses the feature error between the source image and its cyclic reconstruction, accessible in CycleGANs. Let $\hat{F} : T \rightarrow S$ and \hat{D}_S denote the target-to-source model and source domain discriminator, respectively. Confidence is computed by the feature matching loss between s and $\hat{s} = \hat{F}(\hat{G}(s))$, specifically $-\|\hat{D}_S^{(-1)}(s) - \hat{D}_S^{(-1)}(\hat{s})\|_2$ where $\hat{D}_S^{(-1)}$ denotes the penultimate layer feature extractor of \hat{D}_S . (iii) f-AnoGAN [84, 29] merges ALAD and the source residual, $-\|s - \hat{s}\|_2$, though we use just the lat-

ter for their separate assessment.

We also evaluate ablation versions of NHP: (iv) $\gamma = 0$, ignoring FN; (v) $q = 0$, with no data removal in \mathcal{D}^* ; (vi) the linear balance of KNN + γ FN. All unspecified parameters are tuned in the same manner. We also substitute KNN with alternate “distance” measures: (vii) Outside-the-Box (OtB, without K-means) [77] constructs a C -dimensional box (*i.e.*, hyperrectangle) based on the p -th percentile calibration feature elements in Z_q^{*l} . Afterwards, for a sample s with feature $z \in \mathbb{R}^C$, we replace Eq. 7 with the ratio of in-box feature elements. (viii) Residual [76] finds the principal subspace of Z_q^{*l} with explained variance ratio r . We then use the negative ℓ_1 norm of z projected onto the residual subspace orthogonal to this subspace. (ix) GMM [85, 86] fits a Gaussian Mixture Model with c_k clusters, to which afterwards, the log-likelihood (negative surprisal) is used. For all three variants, we appropriately scale the scores before merging with FN. For fair comparison, we perform grid searches to tune respective parameters as well: $p \in \{1, 0.99, 0.975, 0.95, 0.9, 0.8\}$ for OtB, $r \in \{0.99, 0.975, 0.95, 0.925, 0.9, 0.8\}$ for Residual, and $c_k \in \{1, 4, 8, 16, 32, 64\}$ for GMM.

5.2 Main Results

GAN-based anomaly detectors underperform. From Tab. 1, they frequently

Table 2: Further ablations. Mean HRP (% , \uparrow) with NHP parameters fixed at their overall optimum. Declines by +1% from NHP in red.

Method	SRS-to-HE		HO342-to-CD3		HO342-to-CD8		HE-to-ER		HE-to-HER2		HE-to-PR		HE-to-Ki67		Avg.
	Pix2PixHD	VSGD+pNCE	Pix2PixHD	VSGD+pNCE	Pix2PixHD	VSGD+pNCE	CycleGAN	CUT	CycleGAN	CUT	CycleGAN	CUT	CycleGAN	CUT	
NHP ($l = 1$)	49.32 \pm 5.51	37.24 \pm 5.74	40.99 \pm 3.29	46.47 \pm 18.58	26.25 \pm 7.87	31.0 \pm 14.6	69.25 \pm 2.86	62.15 \pm 6.31	51.0 \pm 5.47	43.38 \pm 8.93	68.87 \pm 1.87	57.76 \pm 4.51	67.0 \pm 3.63	47.91 \pm 20.45	49.9
NHP ($k = 1$)	49.6 \pm 5.37	37.24 \pm 5.74	51.06 \pm 3.96	47.8 \pm 16.07	43.96 \pm 5.11	31.56 \pm 14.39	66.16 \pm 2.36	60.9 \pm 6.61	50.98 \pm 5.82	43.22 \pm 8.73	67.62 \pm 2.74	57.12 \pm 5.1	65.21 \pm 3.44	47.0 \pm 20.23	51.39
NHP ($\gamma = -1$)	45.21 \pm 7.93	35.81 \pm 7.57	39.97 \pm 3.27	49.44 \pm 16.39	25.51 \pm 7.95	32.61 \pm 16.42	68.99 \pm 3.05	57.53 \pm 5.3	49.5 \pm 5.1	43.3 \pm 8.66	68.89 \pm 1.9	54.79 \pm 5.33	66.21 \pm 3.33	42.17 \pm 19.79	48.57

display no (HRP=0) or even misalignment (HRP<0) with hallucinations. The standard deviations of HRP across different seeds is significant, reaching up to 46% in worse cases. This highlights the instability of these methods due to reliance on fickle GAN training. Note, ALAD and f-AnoGAN incur higher latency and are only seamlessly compatible with CycleGAN configurations. While ALOCC is free of such constraints, it considerably underperforms. This echoes previous study [83], stating it fails when the discriminator is under- or over-trained. Even when ideal, detection is confined to hallucinations outside the discriminator’s learned target distribution, struggling with hyperrealistic cases.

NHP performs best. Some ablation versions like the GMM and the linear FN/KNN balance are performant, but fall short in certain settings—*e.g.*, NHP (GMM) in HO342 datasets, and NHP (linear) in SRS, both over the Pix2PixHD backbone. In contrast, NHP consistently ranks as either the winner or runner-up (on par with the winner). This justifies our design choices; HRP markedly declined with ablations approaching the vanilla KNN formulation ($\gamma = 0$, $q = 0$). We also confirm the benefits of KNN, with other distance measures like GMM (which assumes Gaussian distributions) or OtB (which reduces to a simple hyperrectangle) yielding inferior results. This is attributed to KNN’s non-parametric nature, as VS feature distributions can be diverse (*cf.* UMAPs of Fig. 4).

Retrospective analysis of NHP parameters. From grid searches, we show the histogram of converged values in Fig. 6, observ-

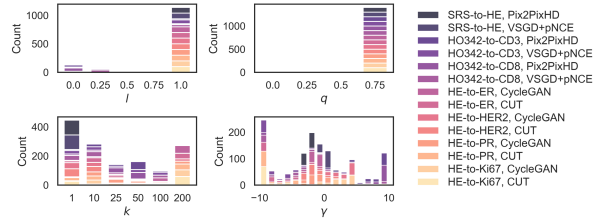


Figure 6: Histograms of converged NHP parameters. Aggregated from 1400 NHPs, color-coded by the 14 settings.

ing the following: (i) The last layer ($l = 1$) is generally the best, but earlier layers ($l \leq 0.25$) sometimes perform better for HO342. Middle layers (usually the bottleneck) are never optimal. (ii) Aggressive truncation ($q = 0.75$) is always preferred. Although a similar idea in image classification showed modest improvement ($\sim 2\%$) by removing erroneous ID data [62], this step is much crucial for VS, as aggressive removals can boost HRP performances by over 20%. (iii) k and γ are highly dispersed.

Except for q , NHP does not consistently choose l , k , and γ , even in the same VS setting, due to variations in validation splits. This corroborates our “no single optimal parameter” hypothesis, further affirmed by the inferior results when fixing parameters to their generally best values ($l = 1$, $k = 1$, $\gamma \approx -1$) in Tab. 2. The grid search is hence integral, as it permits NHP to adapt to each task. Although q was constant, we still recommend conservatively including it in the grid search as it only incurs 1-2 minutes.

Sensitivity test. By aggressive truncation, there is a caveat such that it may fail with smaller \mathcal{D}^* . While our current sample numbers

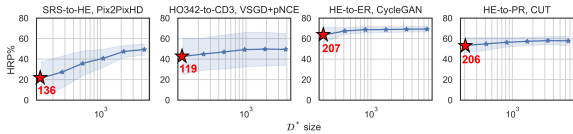


Figure 7: NHP’s sensitivity to \mathcal{D}^* size. We plot mean HRP with confidence intervals representing \pm std.

of 3-7K are reasonable (on par with the minima in [74, 68, 69, 87]), we explore if NHP works with even fewer numbers. For select experiments, we plot mean HRP while downsampling the current \mathcal{D}^* by factors of $\{2, 4, 8, 16, 32\}$. Most NHPs retain performances down to 100-200, an impressive achievement considering that the feature bank (post validation split and truncation) contains fewer than 50 samples. SRS was an exception, suggesting that NHP, while highly robust, is not fail-proof. Nonetheless, NHP remains aligned with hallucinations, maintaining competitiveness down to 1K patches.

5.3 Extension to Advanced Settings

We next evaluate NHP in OOD and adversarial environments (Fig. 8), both real-world vulnerabilities in VS (§3.2). These settings introduce new hallucinogenic factors not seen during self-tuning over training samples. Thus, the goal is to see how NHP fares in harder settings. Recall, the monitor must align with VS prediction, communicating confidence when OOD or adversarially robust, while detecting just for hallucinations.

Setup. For **OOD**, we simulate clinically relevant corruptions to the test set while preserving pathological content. For SRS, we consider six types—(i) additive noise with variable intensity, (ii) contrast jitters, (iii) blurs using a defocus, motion, or zoom kernels, (iv) pixel saturation by setting random small boxes to the maximum value, (v) pixel dropout, and (vi)

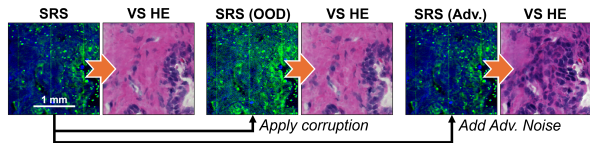


Figure 8: Challenging NHP to its limits. An OOD and PGD attack is shown. Note how the VS is robust to this specific OOD but not to the PGD attack; detection must align with these trends.

Table 3: Harder settings. Mean HRP (%), \uparrow for ALOCC, NHP, and runner-ups, across all VS experiments. Best method in **bold**.

Method	Test set		OOD		Adv. Ex.	
	HRP \uparrow	Val. Gap	HRP \uparrow	Val. Gap	HRP \uparrow	Val. Gap
ALOCC	-0.7 \pm 29.48	-	-3.18 \pm 27.34	-	-6.7 \pm 26.11	-
NHP (GMM)	48.93 \pm 15.07	2.43 \pm 11.99	47.94 \pm 13.61	5.65 \pm 12.68	42.87 \pm 19.34	10.60 \pm 17.32
NHP (linear)	51.58 \pm 14.75	1.23 \pm 10.08	49.57 \pm 12.52	4.29 \pm 10.58	43.52 \pm 17.15	10.3 \pm 16.66
NHP (Ours)	52.4\pm14.3	1.42 \pm 9.61	49.62\pm13.34	3.99 \pm 11.34	44.87\pm16.22	8.75 \pm 16.92

misregistration by slightly offsetting the alignment between channels via affine transformation. These reflect real-world acquisition errors such as instrument failures. For HO342, we similarly apply (i) noise, (ii) blurs, (iii) contrast jitters, and (iv) pixel dropout. For MIST, we consider popular HE corruptions in literature—(i) image compression to JPEG or WebP, (ii) stain color variations, (iii) blurs, and (d) artifacts by superimposing a marker or bubble mask (from [88]).

For **adversarial examples**, we apply Projected Gradient Descent (PGD) [89] to iteratively perturb test sample s into s^{adv} , maximizing the error between $\hat{G}(s^{\text{adv}})$ and t (or $\hat{G}(s)$ if t is unknown to the attacker). Denoting the t -th step as s_t^{adv} with $s_0^{\text{adv}} = s$, we update as follows:

$$s_{t+1}^{\text{adv}} = \Pi \left(s_t^{\text{adv}} + \alpha \cdot \text{sign}(\nabla_s (|\hat{G}(s_t^{\text{adv}}) - \xi|_2^2)) \right),$$

$$s.t. \quad \xi \in \{t, \hat{G}(s)\}, \|s_{t+1}^{\text{adv}} - s\|_p \leq \epsilon,$$
(9)

where ϵ is the perturbation budget, α is the step size, $\nabla_s(\cdot)$ is the gradient w.r.t. s , and $\Pi(\cdot)$ is the projection operator for the l_p bound. While other losses can be used, the

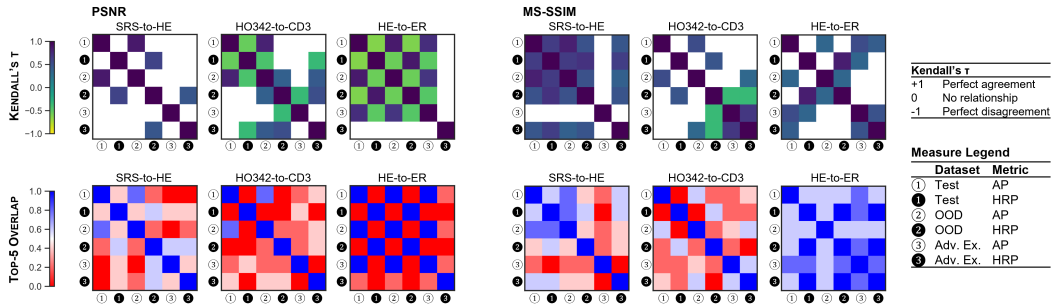


Figure 9: Pairwise correlation of safety measures. We show Kendall’s τ (top row) and overlap ratio (bottom row) across three datasets using PSNR (left) and MS-SSIM (right). White cells are invalid due to high p -values ($p > 0.05$).

pixel-wise ℓ_2 -norm has proven effective (see Fig. 8). We generate diverse examples by randomly drawing $\epsilon \in \{1/255, 4/255, 8/255\}$, $p \in \{2, \infty\}$, and $\xi \in \{t, \hat{G}(s)\}$, per test sample. The step size, α , is fixed at 0.2 for ℓ_2 and $1/255$ for ℓ_∞ . We use $t = 10$ PGD steps for HO342 and MIST, and $t = 50$ for SRS, which we observed to be more resilient.

NHP remains effective, but to a lesser degree. From Tab. 3, NHP performs best overall but shows a drop in HRP in harder settings. To investigate, we quantify the detection gap—the expected HRP decline from the validation subset \mathcal{D}^* used for tuning to these external datasets. Initially, this gap was only 1.42 %, indicating strong generalizability. However, it worsens under corruption and adversarial manipulation, explaining the commensurate decrease in HRP. While NHP is effective, there is potential for improvement by tightening this gap through more complex samples in the self-tuning step, a direction for future work.

5.4 Relationship Between Safety Measures

In this section, we investigate whether VS models with higher average performance (AP), $\mathbb{E}_{(s,t) \in \mathcal{D}_{\text{test}}} [\mathcal{Q}(\hat{G}(s), t)]$, enable better hallucination detection. This is crucial because VS literature reports only AP, whereas real-world de-

ployment hinges on multiple safety measures [90], specifically the ability to both withstand and identify hallucinations. Having established NHP as a strong baseline, we use it as our monitor backbone herein.

Setup. Across our 20 models per dataset, we compare six measures: AP and HRP for test, OOD, and adversarial sets. Each \mathcal{Q} metric is analyzed separately, as AP scores cannot be averaged like HRP due to scale differences. For each measure pair, we compute (i) robust Kendall’s τ [35] for rank correlation and (ii) the overlap ratio of top-5 performers. We display select results in Fig. 9.

AP is not all you need. Correlation matrices vary significantly, with AP often at odds with HRP. For example, the τ between test set AP_{PSNR} and HRP_{PSNR} are -0.54 and -0.63 (moderate anti-correlation) for HO342-to-CD3 and HE-to-ER, respectively, with no top-5 overlap. This trend also appears within the same measure type across datasets, *e.g.*, $\text{HRP}_{\text{MS-SSIM}}$ between OOD and adversarial examples in HO342-to-CD3. Thus, relying solely on AP (or any single metric) risks a false sense of security. This echoes trade-off findings in natural images [91, 92, 93] where improving one robustness metric often undermined others. This is a concern in VS as recent hallucination mitigation methods [4, 6, 7, 9, 10, 16,

[11, 12, 13, 14] do not assess beyond the test set AP. We thus advocate for a re-evaluation of VS practices to incorporate holistic evaluations, particularly HRP.

5.5 Limitations and Future Work

Some current limitations also inspire future developments:

(i) Assumption violations: While modern VS practices can typically meet the assumptions in §4, exceptions exist, such as with commercial black-box VS models or practical constraints preventing data from adjacent sections. (ii) Finer attribution: NHP provides a scalar confidence per patch, sufficient for WSIs and matching the interpretability resolution of multiple instance learning (MIL) [94, 95, 96]. However, finer resolution may be desirable for “needle-in-a-haystack” tasks like detecting micro-metastases [97]. One approach is to omit spatial downscaling in Eq. 3 and return a map instead. Categorizing hallucination source (*e.g.*, epistemic *vs.* aleatoric [98]) or threat level could also aid informed decision-making. We reserve these goals for future work. (iii) Hallucination hypothesis: We recognize the critical need for a more accurate metric, which extends beyond our work to the broader VS community.

6 Conclusions

In this work, we studied hallucination detection for VS, contributing in mainly three dimensions. First, we coherently established the problem with a summary of hallucination causes, an evaluation metric, and clarification with related detection tasks. Second, we introduced a novel hallucination detection method, NHP, with extensive validation. Third, we revealed new insights, particularly on the evaluation of VS robustness. Together, as the first work of its kind, this work provides a useful

framework to assess hallucinations in VS images that could prove useful across the biomedical research and clinical landscape.

References

- [1] S. E. Mills, D. Carter, J. K. Greenon, V. E. Reuter, and M. H. Stoler, *Sternberg’s diagnostic surgical pathology*. Lippincott Williams & Wilkins, 2012.
- [2] D. Mayerich, M. J. Walsh, A. Kadjacsy-Balla, P. S. Ray, S. M. Hewitt, and R. Bhargava, “Stain-less staining for computed histopathology,” *Technology*, vol. 3, no. 01, pp. 27–31, 2015.
- [3] K. de Haan, Y. Zhang, J. E. Zuckerman, T. Liu, A. E. Sisk, M. F. Diaz, K.-Y. Jen, A. Nobori, S. Liou, S. Zhang, *et al.*, “Deep learning-based transformation of h&e stained tissues into special stains,” *Nat. Commun.*, vol. 12, no. 1, pp. 1–13, 2021.
- [4] S. Liu, B. Zhang, Y. Liu, A. Han, H. Shi, T. Guan, and Y. He, “Unpaired stain transfer using pathology-consistent constrained generative adversarial networks,” *IEEE Trans. Med. Imaging*, vol. 40, no. 8, pp. 1977–1989, 2021.
- [5] S. Liu, C. Zhu, F. Xu, X. Jia, Z. Shi, and M. Jin, “Bci: Breast cancer immunohistochemical image generation through pyramid pix2pix,” in *IEEE Conf. Comput. Vis. Pattern Recog. Worksh.*, pp. 1814–1823, IEEE, 2022.
- [6] B. Zeng, Y. Lin, Y. Wang, Y. Chen, J. Dong, X. Li, and Y. Zhang, “Semi-supervised pr virtual staining for breast histopathological images,” in *Int. Conf. Med. Image Comput. Comput. Assist. Interv.*, pp. 232–241, Springer, 2022.

- [7] Y. Lin, B. Zeng, Y. Wang, Y. Chen, Z. Fang, J. Zhang, X. Ji, H. Wang, and Y. Zhang, “Unpaired multi-domain stain transfer for kidney histopathological images,” in *AAAI Conf. Artif. Intell.*, vol. 36, pp. 1630–1637, 2022.
- [8] R. Zhang, Y. Cao, Y. Li, Z. Liu, J. Wang, J. He, C. Zhang, X. Sui, P. Zhang, L. Cui, *et al.*, “Mvfstain: multiple virtual functional stain histopathology images generation based on specific domain mapping,” *Med. Image Anal.*, vol. 80, p. 102520, 2022.
- [9] J. Boyd, I. Villa, M.-C. Mathieu, E. Deutsch, N. Paragios, M. Vakalopoulou, and S. Christodoulidis, “Region-guided cyclegans for stain transfer in whole slide images,” in *Int. Conf. Med. Image Comput. Comput. Assist. Interv.*, pp. 356–365, Springer, 2022.
- [10] F. Li, Z. Hu, W. Chen, and A. Kak, “Adaptive supervised patchnce loss for learning h&e-to-ihc stain translation with inconsistent groundtruth image pairs,” in *Int. Conf. Med. Image Comput. Comput. Assist. Interv.*, pp. 632–641, Springer, 2023.
- [11] J. Li, J. Dong, S. Huang, X. Li, J. Jiang, X. Fan, and Y. Zhang, “Virtual immunohistochemistry staining for histological images assisted by weakly-supervised learning,” in *IEEE Conf. Comput. Vis. Pattern Recog.*, pp. 11259–11268, 2024.
- [12] F. Chen, R. Zhang, B. Zheng, Y. Sun, J. He, and W. Qin, “Pathological semantics-preserving learning for h&e-to-ihc virtual staining,” *Int. Conf. Med. Image Comput. Comput. Assist. Interv.*, 2024.
- [13] S. Wang, Z. Zhang, H. Yan, M. Xu, and G. Wang, “Mix-domain contrastive learning for unpaired h&e-to-ihc stain translation,” *arXiv preprint arXiv:2406.11799*, 2024.
- [14] L. Wei, S. Hua, S. Zhang, and X. Zhang, “Derestainer: H&e to ihc pathological image translation via decoupled staining channels,” *Int. Conf. Med. Image Comput. Comput. Assist. Interv.*, 2024.
- [15] K. Liu, B. Li, W. Wu, C. May, O. Chang, S. Knezevich, L. Reisch, J. Elmore, and L. Shapiro, “Vsgd-net: Virtual staining guided melanocyte detection on histopathological images,” in *IEEE Winter Conf. Appl. Comput. Vis.*, pp. 1918–1927, 2023.
- [16] J. Ma and H. Chen, “Efficient supervised pretraining of swin-transformer for virtual staining of microscopy images,” *IEEE Trans. Med. Imaging*, 2023.
- [17] N. Bayramoglu, M. Kaakinen, L. Eklund, and J. Heikkila, “Towards virtual h&e staining of hyperspectral lung histology images using conditional generative adversarial networks,” in *IEEE Int. Conf. Comput. Vis. Worksh.*, pp. 64–71, 2017.
- [18] Y. Rivenson, T. Liu, Z. Wei, Y. Zhang, K. de Haan, and A. Ozcan, “Phasestain: the digital staining of label-free quantitative phase microscopy images using deep learning,” *Light Sci. Appl.*, vol. 8, no. 1, p. 23, 2019.
- [19] Y. Rivenson, H. Wang, Z. Wei, K. de Haan, Y. Zhang, Y. Wu, H. Günaydin, J. E. Zuckerman, T. Chong, A. E. Sisk, *et al.*, “Virtual histological staining of unlabelled tissue-autofluorescence images via deep

- learning,” *Nat. Biomed. Eng.*, vol. 3, no. 6, pp. 466–477, 2019.
- [20] M. Schnell, S. Mittal, K. Falahkheirkhah, A. Mittal, K. Yeh, S. Kenkel, A. Kajdacsy-Balla, P. S. Carney, and R. Bhargava, “All-digital histopathology by infrared-optical hybrid microscopy,” *PNAS*, vol. 117, no. 7, pp. 3388–3396, 2020.
- [21] L. Shi, I. H. Wong, C. T. Lo, L. W. Tsui, and T. T. Wong, “Unsupervised multiple virtual histological staining from label-free autofluorescence images,” in *IEEE Int. Symp. Biomed. Imaging*, pp. 1–5, IEEE, 2023.
- [22] G. Wölflein, I. H. Um, D. J. Harrison, and O. Arandjelović, “Hoechstgan: virtual lymphocyte staining using generative adversarial networks,” in *IEEE Winter Conf. Appl. Comput. Vis.*, pp. 4997–5007, 2023.
- [23] L. Huang, Y. Li, N. Pillar, T. K. Haran, W. D. Wallace, and A. Ozcan, “Autonomous quality and hallucination assessment for virtual tissue staining and digital pathology,” *arXiv preprint arXiv:2404.18458*, 2024.
- [24] M. Ounissi, I. Sarbout, J.-P. Hugot, C. Martinez-Vinson, D. Berrebi, and D. Racoceanu, “Scalable, trustworthy generative model for virtual multi-staining from h&e whole slide images,” *arXiv preprint arXiv:2407.00098*, 2024.
- [25] P. Isola, J.-Y. Zhu, T. Zhou, and A. A. Efros, “Image-to-image translation with conditional adversarial networks,” in *IEEE Conf. Comput. Vis. Pattern Recog.*, pp. 1125–1134, 2017.
- [26] J.-Y. Zhu, T. Park, P. Isola, and A. A. Efros, “Unpaired image-to-image translation using cycle-consistent adversarial networks,” in *IEEE Int. Conf. Comput. Vis.*, pp. 2223–2232, 2017.
- [27] H. Zenati, M. Romain, C.-S. Foo, B. Lecouat, and V. Chandrasekhar, “Adversarially learned anomaly detection,” in *IEEE Int. Conf. Data Min.*, pp. 727–736, IEEE, 2018.
- [28] M. Sabokrou, M. Khalooei, M. Fathy, and E. Adeli, “Adversarially learned one-class classifier for novelty detection,” in *IEEE Conf. Comput. Vis. Pattern Recog.*, pp. 3379–3388, 2018.
- [29] T. Schlegl, P. Seeböck, S. M. Waldstein, G. Langs, and U. Schmidt-Erfurth, “fanogan: Fast unsupervised anomaly detection with generative adversarial networks,” *Med. Image Anal.*, vol. 54, pp. 30–44, 2019.
- [30] T.-C. Wang, M.-Y. Liu, J.-Y. Zhu, A. Tao, J. Kautz, and B. Catanzaro, “High-resolution image synthesis and semantic manipulation with conditional gans,” in *IEEE Conf. Comput. Vis. Pattern Recog.*, pp. 8798–8807, 2018.
- [31] S. Bhadra, V. A. Kelkar, F. J. Brooks, and M. A. Anastasio, “On hallucinations in tomographic image reconstruction,” *IEEE Trans. Med. Imaging*, vol. 40, no. 11, pp. 3249–3260, 2021.
- [32] M. Tivnan, S. Yoon, Z. Chen, X. Li, D. Wu, and Q. Li, “Hallucination index: An image quality metric for generative reconstruction models,” in *Int. Conf. Med. Image Comput. Comput. Assist. Interv.*, pp. 449–458, Springer, 2024.
- [33] Z. Wang, E. P. Simoncelli, and A. C. Bovik, “Multiscale structural similarity

- for image quality assessment,” in *ACSSC*, vol. 2, pp. 1398–1402, Ieee, 2003.
- [34] R. Zhang, P. Isola, A. A. Efros, E. Shechtman, and O. Wang, “The unreasonable effectiveness of deep features as a perceptual metric,” in *IEEE Conf. Comput. Vis. Pattern Recog.*, pp. 586–595, 2018.
- [35] M. G. Kendall, “A new measure of rank correlation,” *Biometrika*, vol. 30, no. 1-2, pp. 81–93, 1938.
- [36] A. M. Stuart, “Inverse problems: a bayesian perspective,” *Acta Numer.*, vol. 19, pp. 451–559, 2010.
- [37] C. Zhang and B. Jin, “Probabilistic residual learning for aleatoric uncertainty in image restoration,” *arXiv preprint arXiv:1908.01010*, 2019.
- [38] M. Tölle, M.-H. Laves, and A. Schläfer, “A mean-field variational inference approach to deep image prior for inverse problems in medical imaging,” in *Med. Imaging Deep Learn.*, pp. 745–760, PMLR, 2021.
- [39] P. Ebel, V. S. F. Garnot, M. Schmitt, J. D. Wegner, and X. X. Zhu, “Uncrtaints: Uncertainty quantification for cloud removal in optical satellite time series,” in *IEEE Conf. Comput. Vis. Pattern Recog.*, pp. 2086–2096, 2023.
- [40] L. Mescheder, S. Nowozin, and A. Geiger, “The numerics of gans,” in *Adv. Neural Inform. Process. Syst.*, pp. 1826–1836, Curran Associates, Inc., 2018.
- [41] H. Thanh-Tung and T. Tran, “Catastrophic forgetting and mode collapse in gans,” in *Proc. Int. Jt. Conf. Neural Netw.*, pp. 1–10, IEEE, 2020.
- [42] J. P. Cohen, M. Luck, and S. Honari, “Distribution matching losses can hallucinate features in medical image translation,” in *Int. Conf. Med. Image Comput. Comput. Assist. Interv.*, pp. 529–536, Springer, 2018.
- [43] O. Patashnik, D. Danon, H. Zhang, and D. Cohen-Or, “Balagan: cross-modal image translation between imbalanced domains,” in *IEEE Conf. Comput. Vis. Pattern Recog.*, pp. 2659–2667, 2021.
- [44] J. Mehrer, C. J. Spoerer, N. Kriegeskorte, and T. C. Kietzmann, “Individual differences among deep neural network models,” *Nat. Commun.*, vol. 11, no. 1, p. 5725, 2020.
- [45] A. D’Amour, K. Heller, D. Moldovan, B. Adlam, B. Alipanahi, A. Beutel, C. Chen, J. Deaton, J. Eisenstein, M. D. Hoffman, *et al.*, “Underspecification presents challenges for credibility in modern machine learning,” *J. Mach. Learn. Res.*, vol. 23, no. 226, pp. 1–61, 2022.
- [46] L. Breiman, “Statistical modeling: The two cultures (with comments and a rejoinder by the author),” *Statistical Science*, vol. 16, no. 3, pp. 199–231, 2001.
- [47] M.-Y. Liu, T. Breuel, and J. Kautz, “Unsupervised image-to-image translation networks,” in *Adv. Neural Inform. Process. Syst.*, pp. 700–708, 2017.
- [48] G. Lu, Z. Zhou, Y. Song, K. Ren, and Y. Yu, “Guiding the one-to-one mapping in cycleGAN via optimal transport,” in *AAAI Conf. Artif. Intell.*, vol. 33, pp. 4432–4439, 2019.
- [49] Z. Shen, S. K. Zhou, Y. Chen, B. Georgescu, X. Liu, and T. Huang,

- “One-to-one mapping for unpaired image-to-image translation,” in *IEEE Winter Conf. Appl. Comput. Vis.*, pp. 1170–1179, 2020.
- [50] F. M. Howard, J. Dolezal, S. Kochanny, J. Schulte, H. Chen, L. Heij, D. Huo, R. Nanda, O. I. Olopade, J. N. Kather, *et al.*, “The impact of site-specific digital histology signatures on deep learning model accuracy and bias,” *Nat. Commun.*, vol. 12, no. 1, p. 4423, 2021.
- [51] J.-H. Oh, K. Falahkheirkhah, and R. Bhargava, “Are we ready for out-of-distribution detection in digital pathology?,” *Int. Conf. Med. Image Comput. Comput. Assist. Interv.*, 2024.
- [52] M. Arjovsky, L. Bottou, I. Gulrajani, and D. Lopez-Paz, “Invariant risk minimization,” *arXiv preprint arXiv:1907.02893*, 2019.
- [53] D. Teney, M. Peyrard, and E. Abbasnejad, “Predicting is not understanding: Recognizing and addressing underspecification in machine learning,” in *Eur. Conf. Comput. Vis.*, pp. 458–476, Springer, 2022.
- [54] N. Ghaffari Laleh, D. Truhn, G. P. Veldhuizen, T. Han, M. van Treeck, R. D. Buelow, R. Langer, B. Dislich, P. Boor, V. Schulz, *et al.*, “Adversarial attacks and adversarial robustness in computational pathology,” *Nat. Commun.*, vol. 13, no. 1, p. 5711, 2022.
- [55] C.-Y. Yeh, H.-W. Chen, S.-L. Tsai, and S.-D. Wang, “Disrupting image-translation-based deepfake algorithms with adversarial attacks,” in *IEEE Winter Conf. Appl. Comput. Vis. Worksh.*, pp. 53–62, 2020.
- [56] C. Yang, L. Ding, Y. Chen, and H. Li, “Defending against gan-based deepfake attacks via transformation-aware adversarial faces,” in *IEEE Proc. Int. Jt. Conf. Neural Netw.*, pp. 1–8, IEEE, 2021.
- [57] X. Liu, J. Liu, Y. Bai, J. Gu, T. Chen, X. Jia, and X. Cao, “Watermark vaccine: Adversarial attacks to prevent watermark removal,” in *Eur. Conf. Comput. Vis.*, pp. 1–17, Springer, 2022.
- [58] A. Malinin, B. Mlodozieniec, and M. Gales, “Ensemble distribution distillation,” in *Int. Conf. Learn. Represent.*, 2020.
- [59] J. Van Amersfoort, L. Smith, Y. W. Teh, and Y. Gal, “Uncertainty estimation using a single deep deterministic neural network,” in *Int. Conf. Mach. Learn.*, pp. 9690–9700, PMLR, 2020.
- [60] J. Postels, M. Segù, T. Sun, L. D. Sieber, L. Van Gool, F. Yu, and F. Tombari, “On the practicality of deterministic epistemic uncertainty,” in *Int. Conf. Mach. Learn.*, pp. 17870–17909, PMLR, 2022.
- [61] J. Yang, K. Zhou, Y. Li, and Z. Liu, “Generalized out-of-distribution detection: A survey,” *Int. J. Comput. Vis.*, pp. 1–28, 2024.
- [62] J. Guérin, K. Delmas, R. Ferreira, and J. Guiochet, “Out-of-distribution detection is not all you need,” in *AAAI Conf. Artif. Intell.*, vol. 37, pp. 14829–14837, 2023.
- [63] P. F. Jaeger, C. T. Lüth, L. Klein, and T. J. Bungert, “A call to reflect on evaluation practices for failure detection in image classification,” in *Int. Conf. Learn. Represent.*, 2023.
- [64] R. Averly and W.-L. Chao, “Unified out-of-distribution detection: A model-

- specific perspective,” in *Int. Conf. Comput. Vis.*, pp. 1453–1463, 2023.
- [65] C. Jun, D. Luan, S. Zhang, Y. Pei, Y. Zhang, D. Zhao, S. Shen, and Q. Chen, “The devil is in the wrongly-classified samples: Towards unified open-set recognition,” in *Int. Conf. Learn. Represent.*, 2023.
- [66] S. Tonks, C. Nguyer, S. Hood, R. Musso, C. Hopely, S. Titus, M. Doan, I. Styles, and A. Krull, “Can virtual staining for high-throughput screening generalize?,” *arXiv preprint arXiv:2407.06979*, 2024.
- [67] L. McInnes, J. Healy, N. Saul, and L. Großberger, “Umap: Uniform manifold approximation and projection,” *J. Open Source Softw.*, vol. 3, no. 29, 2018.
- [68] Y. Sun, Y. Ming, X. Zhu, and Y. Li, “Out-of-distribution detection with deep nearest neighbors,” in *Int. Conf. Mach. Learn.*, pp. 20827–20840, PMLR, 2022.
- [69] J. Park, Y. G. Jung, and A. B. J. Teoh, “Nearest neighbor guidance for out-of-distribution detection,” in *IEEE Conf. Comput. Vis. Pattern Recog.*, pp. 1686–1695, 2023.
- [70] A. R. Dhamija, M. Günther, and T. E. Boult, “Reducing network agnostophobia,” in *Adv. Neural Inform. Process. Syst.*, pp. 9175–9186, 2018.
- [71] J. Tack, S. Mo, J. Jeong, and J. Shin, “Csi: novelty detection via contrastive learning on distributionally shifted instances,” in *Adv. Neural Inform. Process. Syst.*, pp. 11839–11852, 2020.
- [72] Y. Yu, S. Shin, S. Lee, C. Jun, and K. Lee, “Block selection method for using feature norm in out-of-distribution detection,” in *IEEE Conf. Comput. Vis. Pattern Recog.*, pp. 15701–15711, 2023.
- [73] J. Park, J. C. L. Chai, J. Yoon, and A. B. J. Teoh, “Understanding the feature norm for out-of-distribution detection,” in *IEEE Conf. Comput. Vis. Pattern Recog.*, pp. 1557–1567, 2023.
- [74] K. Lee, K. Lee, H. Lee, and J. Shin, “A simple unified framework for detecting out-of-distribution samples and adversarial attacks,” in *Adv. Neural Inform. Process. Syst.*, pp. 7167–7177, 2018.
- [75] E. D. C. Gomes, F. Alberge, P. Duhamel, and P. Piantanida, “Igeood: An information geometry approach to out-of-distribution detection,” in *Int. Conf. Learn. Represent.*, 2022.
- [76] H. Wang, Z. Li, L. Feng, and W. Zhang, “Vim: Out-of-distribution with virtual-logit matching,” in *IEEE Conf. Comput. Vis. Pattern Recog.*, pp. 4921–4930, 2022.
- [77] T. A. Henzinger, A. Lukina, and C. Schilling, “Outside the box: Abstraction-based monitoring of neural networks,” in *Eur. Conf. Artif. Intell.*, vol. 325, 2020.
- [78] D. Hendrycks, M. Mazeika, and T. Dietterich, “Deep anomaly detection with outlier exposure,” in *Int. Conf. Learn. Represent.*, 2019.
- [79] J. Johnson, M. Douze, and H. Jégou, “Billion-scale similarity search with gpus,” *IEEE Trans Big Data*, vol. 7, no. 3, pp. 535–547, 2019.
- [80] K. Falahkheirkhah, S. S. Mukherjee, S. Gupta, L. Herrera-Hernandez, M. R. McCarthy, R. E. Jimenez, J. C. Cheville, and R. Bhargava, “Accelerating cancer histopathology workflows with chemical

- imaging and machine learning,” *Cancer Research Commun.*, vol. 3, no. 9, pp. 1875–1887, 2023.
- [81] A. Andonian, T. Park, B. Russell, P. Isola, J.-Y. Zhu, and R. Zhang, “Contrastive feature loss for image prediction,” in *Int. Conf. Comput. Vis. Worksh.*, pp. 1934–1943, 2021.
- [82] T. Park, A. A. Efros, R. Zhang, and J.-Y. Zhu, “Contrastive learning for unpaired image-to-image translation,” in *Eur. Conf. Comput. Vis.*, pp. 319–345, Springer, 2020.
- [83] M. Z. Zaheer, J.-h. Lee, M. Astrid, and S.-I. Lee, “Old is gold: Redefining the adversarially learned one-class classifier training paradigm,” in *IEEE Conf. Comput. Vis. Pattern Recog.*, pp. 14183–14193, 2020.
- [84] T. Schlegl, P. Seeböck, S. M. Waldstein, U. Schmidt-Erfurth, and G. Langs, “Unsupervised anomaly detection with generative adversarial networks to guide marker discovery,” in *Inf. Process. Med. Imaging*, pp. 146–157, Springer, 2017.
- [85] N. A. Ahuja, I. Ndiour, T. Kalyanpur, and O. Tickoo, “Probabilistic modeling of deep features for out-of-distribution and adversarial detection,” *arXiv preprint arXiv:1909.11786*, 2019.
- [86] J. Yang, K. Zhou, and Z. Liu, “Full-spectrum out-of-distribution detection,” *Int. J. Comput. Vis.*, vol. 131, no. 10, pp. 2607–2622, 2023.
- [87] J.-H. Kim, S. Yun, and H. O. Song, “Neural relation graph: A unified framework for identifying label noise and outlier data,” in *Adv. Neural Inform. Process. Syst.*, 2023.
- [88] Y. Zhang, Y. Sun, H. Li, S. Zheng, C. Zhu, and L. Yang, “Benchmarking the robustness of deep neural networks to common corruptions in digital pathology,” in *Med. Image Comput. Comput. Assist. Interv.*, pp. 242–252, Springer, 2022.
- [89] A. Madry, A. Makelov, L. Schmidt, D. Tsipras, and A. Vladu, “Towards deep learning models resistant to adversarial attacks,” in *Int. Conf. Learn. Represent.*, 2018.
- [90] D. Hendrycks, N. Carlini, J. Schuman, and J. Steinhardt, “Unsolved problems in ml safety,” *arXiv preprint arXiv:2109.13916*, 2021.
- [91] D. Tsipras, S. Santurkar, L. Engstrom, A. Turner, and A. Madry, “Robustness may be at odds with accuracy,” in *Int. Conf. Learn. Represent.*, no. 2019, 2019.
- [92] S. Chun, S. J. Oh, S. Yun, D. Han, J. Choe, and Y. Yoo, “An empirical evaluation on robustness and uncertainty of regularization methods,” in *Int. Conf. Mach. Learn. Worksh.*, 2019.
- [93] D. Hendrycks, A. Zou, M. Mazeika, L. Tang, B. Li, D. Song, and J. Steinhardt, “Pixmix: Dreamlike pictures comprehensively improve safety measures,” in *IEEE Conf. Comput. Vis. Pattern Recog.*, pp. 16783–16792, 2022.
- [94] M. Ilse, J. Tomczak, and M. Welling, “Attention-based deep multiple instance learning,” in *Int. Conf. Mach. Learn.*, pp. 2127–2136, 2018.
- [95] S. Kapse, P. Pati, S. Das, J. Zhang, C. Chen, M. Vakalopoulou, J. Saltz, D. Samaras, R. R. Gupta, and P. Prasanna, “Si-mil: Taming deep mil for self-interpretability in gigapixel

- histopathology,” in *IEEE Conf. Comput. Vis. Pattern Recog.*, pp. 11226–11237, 2024.
- [96] A. H. Song, R. J. Chen, T. Ding, D. F. Williamson, G. Jaume, and F. Mahmood, “Morphological prototyping for unsupervised slide representation learning in computational pathology,” in *IEEE Conf. Comput. Vis. Pattern Recog.*, pp. 11566–11578, 2024.
- [97] J.-G. Yu, Z. Wu, Y. Ming, S. Deng, Y. Li, C. Ou, C. He, B. Wang, P. Zhang, and Y. Wang, “Prototypical multiple instance learning for predicting lymph node metastasis of breast cancer from whole-slide pathological images,” *Med. Image Anal.*, vol. 85, p. 102748, 2023.
- [98] E. Hüllermeier and W. Waegeman, “Aleatoric and epistemic uncertainty in machine learning: An introduction to concepts and methods,” *Mach. Learn.*, vol. 110, no. 3, pp. 457–506, 2021.